RSC Advances

PAPER

View Article Online
View Journal | View Issue

Cite this: *RSC Adv.*, 2023, **13**, 6630

Mechanisms of chemical-reaction-induced tensile deformation of an Fe/Ni/Cr alloy revealed by reactive atomistic simulations†

Yang Wang,‡*[ab] Haoyu Zhao,‡[b] Chang Liu,[b] Yusuke Ootani,[b] Nobuki Ozawa[bc] and Momoji Kubo *[bc]

High entropy alloys (HEAs) have demonstrated excellent potential in various applications owing to the unique properties. One of the most critical issues of HEAs is the stress corrosion cracking (SCC) which limits its reliability in practical applications. However, the SCC mechanisms have not been fully understood yet because of the difficulty of experimental measuring of atomic-scale deformation mechanisms and surface reactions. In this work, we conduct atomistic uniaxial tensile simulations using an FCC-type $Fe_{40}Ni_{40}Cr_{20}$ alloy as a typical simplification of normal HEAs, in order to reveal how a corrosive environment such as high-temperature/pressure water affects the tensile behaviors and deformation mechanisms. In a vacuum, we observe the generation of layered HCP phases in an FCC matrix during tensile simulation induced by the formation of Shockley partial dislocations from surface and grain boundaries. While, in the corrosive environment of high-temperature/pressure water, the alloy surface is oxidized by chemical reactions with water and this oxide surface layer can suppress the formation of Shockley partial dislocation as well as the resulting FCC-to-HCP phase transition; instead, a BCC phase is preferred to generate in the FCC matrix for releasing the tensile stress and stored elastic energy, leading to a reduced ductility as the BCC phase is typically more brittle than the FCC and HCP. Overall, the deformation mechanism of the FeNiCr alloy is changed by the presence of a high-temperature/pressure water environment—from FCC-to-HCP phase transition in vacuum to FCC-to-BCC phase transition in water. This theoretical fundamental study may contribute to the further improvement of HEAs with high resistance to SCC in experiments.

Received 6th November 2022
Accepted 3rd February 2023

DOI: 10.1039/d2ra07039a

rsc.li/rsc-advances

1. Introduction

High-entropy alloys (HEAs), a kind of novel alloy formed by mixing equal or relatively large proportions of several elements, have attracted much academic and industrial attention since they were first developed in 2004.[1–4] HEAs exhibit many unique advantages such as high strength and high resistance to corrosion/wear, compared with conventional alloys. These excellent properties make HEAs widely expected as the structural material used in the high-temperature and corrosive environments, *e.g.*, high-temperature and high-pressure water environment in power plants.

However, in the presence of mechanical stress, fatal destruction of HEAs may occur due to the stress corrosion cracking (SCC) phenomenon, even though HEAs have good corrosion resistance in stress-free conditions. For example, Dong *et al.* have experimentally confirmed the SCC initiation of $Fe_{28}Ni_{27}Mn_{27}Cr_{18}$ HEA in high-temperature hydrogenated water environment.[5] Mizumachi *et al.* observed the propagation feature of fatigue cracks in $Fe_{20}Cr_{20}Ni_{20}Mn_{20}Co_{20}$ HEA.[6] Thurston *et al.* studied the SCC propagation mechanism of CrMnFeCoNi HEAs and they reported a change of crack propagation mechanism from transgranular crack propagation at room temperature to intergranular-dominated failure at lower temperatures.[7] To further improve the reliability of HEAs and expand its applications, in-deep insights into the SCC mechanisms of HEAs are strongly desired, comprising atomic-scale deformation mechanisms and chemical reactions with corrosive environments. Nevertheless, the SCC mechanisms have not been elucidated at all because the highly random atomic arrangement of HEAs makes the experimental measuring/observation of the atomic-scale deformation process as well as chemical reactions more difficult than that for the conventional alloys.

[a]*Research Institute of Frontier Science, Southwest Jiaotong University, No. 111, North Section 1, Second Ring Road, Chengdu, Sichuan, 610031, China. E-mail: yang.wang@swjtu.edu.cn*

[b]*Institute for Materials Research, Tohoku University, 2-1-1 Katahira, Aoba-ku, Sendai 980-8577, Japan. E-mail: momoji@tohoku.ac.jp*

[c]*New Industry Creation Hatchery Center, Tohoku University, 6-6-10 Aoba, Aramaki, Aoba-ku, Sendai 980-8579, Japan*

† Electronic supplementary information (ESI) available. See DOI: https://doi.org/10.1039/d2ra07039a

‡ These authors contributed equally to this work.

Molecular dynamics (MD) simulation is a normal approach to study and clarify the atomic-scale behaviors and mechanisms. In MD simulations, empirical atomic potentials (namely, force field) are used to describe the interactions among atoms, *e.g.*, Lennard-Jones and Morse potentials. For metals and alloys, their atomic interactions are generally described well by the embedded atom method (EAM)[8] and its extensions.[9] For example, EAM has been used to study the superelastic properties of BCC-type nanowires[10] and migration mechanisms of deformation twins.[11] However, EAM and related potentials cannot deal with the chemical reactions, so that they are not suitable for studying the SCC problems. On the other hand, first-principles MD simulations can accurately describe the chemical reactions and even the electronic states, whereas it is not able to simulate the deformation process owing to the huge computational costs. As a compromise way for simulating both the chemical reactions and material deformation mechanisms, the reactive force field (ReaxFF)[12,13] is proposed in recent decades. ReaxFF is a kind of bond-order-based potential and is able to describe the bond formation/dissociation with good accuracy and low computational cost if well-trained parameters are employed. ReaxFF has been widely used to study chemical reactions of a large variety of material systems such as the carbon/silicon-based solid lubricants,[14–19] metals,[20] ceramics,[21] biomolecules,[22,23] and polymers,[24,25] showing excellent validities. In this work, we conduct ReaxFF-based MD simulations to shed lights on the SCC mechanisms of HEAs in corrosive environment.

2. Methodology

There are various types of HEAs depending on the added element species and element proportions, while the HEAs with face-centered cubic (FCC) structure containing Fe, Ni, and Cr are the most widely used types due to the high ductility and corrosion resistance.[7,26,27] In this work, we use an FCC-type $Fe_{40}Ni_{40}Cr_{20}$ alloy (consisting of 40% Fe, 40% Ni, and 20% Cr) as a typical simplification model of normal HEAs to study the SCC mechanisms. The simulation model of $Fe_{40}Ni_{40}Cr_{20}$ alloy is shown in Fig. 1. Three-dimension periodic boundary condition (PBC) with a cell size of $54 \times 147 \times 141$ Å^3 are used in this work. Here a slab model of $Fe_{40}Ni_{40}Cr_{20}$ alloy with two grain boundaries (GB) of Σ37 (610) is used (one is at the middle and another one is at the cell edge). This grain boundary is chosen as it is a well-balanced choice: Σ37 (610) is neither too unstable to clearly keep the borderline structure, nor too stable so that we cannot easily observe the focused phenomenon such as cracking (see Fig. S1 in ESI† for details). We create a pre-crack with a height of 30 Å and width of 22 Å at the middle GB to observe the crack propagation in the limited simulation time scale. Thickness of this $Fe_{40}Ni_{40}Cr_{20}$ alloy slab is 107 Å. To study the SCC mechanism, tensile simulations of $Fe_{40}Ni_{40}Cr_{20}$ alloy are performed in two environments: a non-corrosive vacuum and a corrosive high-temperature/pressure water environment. In this simulation, a partial NPT ensemble is employed: the system temperature is fixed at 600 K, while pressures of only x and y directions are kept at 15 MPa. The density of water is 0.66 g cm^{-3} which is the standard density in such conditions. While, for the vacuum environment, the system temperature is also set to 600 K to ensure a same simulation condition.

The above tensile simulations are conducted by using our originally developed MD simulator Laskyo.[28] ReaxFF potential is used to describe the atomic interactions and chemical reactions. Here, the parameters for Fe/Cr/H_2O system are picked directly from the previous studies.[29,30] For the nickel, there are available parameters for Ni/Fe,[31] whereas the parameters for Ni/Cr and Ni/H_2O are lacking and hence should be developed in this research. Details regarding the parameter training methods and results are shown in the Fig. S2 of ESI.† Before tensile simulations, we perform relaxation simulation of the slab models in both vacuum and water environments at a temperature of 5 K and a pressure of 15 MPa, and then the temperature is slowly raised up to 600 K. In the MD tensile simulations, uniaxial tensile strain is applied to the z direction of each model with a constant strain rate of 10^9 s^{-1} and a timestep of 0.25 fs/step. All uniaxial tensile simulations are conducted for 400 000 steps. Velocity-Verlet algorithm[32,33] is used to evolve the atoms. The system temperature and pressure are controlled by the Nose–Hoover chain method.[34] The simulation snapshots are viewed and created by the OVITO software.[35]

3. Results and discussion

Fig. 2 shows the stress–strain curves of $Fe_{40}Ni_{40}Cr_{20}$ alloy during the tensile simulations in both vacuum and high-temperature/pressure water environment. As a consequence, we observe that the $Fe_{40}Ni_{40}Cr_{20}$ alloy in vacuum shows a little lower elastic modulus (slope of the left-side elastic region) but higher ductility (stress value of the right-side plastic region) than those in water environment. Fig. 3 shows atomic shear strain of $Fe_{40}Ni_{40}Cr_{20}$ alloy during tensile simulation in (a) vacuum and (b) high-temperature/pressure water environment. Initially, atomic strains in either vacuum or water environments are almost zero. In the case of vacuum, layered strain bands begin to generate from the grain boundary and surface at the strain of 5.50%, and then the layered shear bands become thick while more and more layered strain bands are generated at the tensile strain of 8.50%, as shown in Fig. 3a. In the case of high temperature and pressure water, atomic strains of the surface atoms become very large at the strain of 5.50% indicating a structural change of surface (Fig. 3b). Meanwhile, layered strain bands are not observed, while instead the atomic shear strain concentrate around the grain boundary. When the tensile strain increases to 8.50%, a large block of high-strain region is observed at the grain boundary. The above results demonstrate the different deformation mechanisms of $Fe_{40}Ni_{40}Cr_{20}$ alloy in vacuum and water environments.

To clarify the above different deformation mechanisms, the atomic structures are investigated in details. The atomic structure results of $Fe_{40}Ni_{40}Cr_{20}$ alloy in vacuum are shown in Fig. 4a where the atoms in face-centered cubic (FCC), body-centered cubic (BCC), and hexagonal closest packed (HCP) phases are assigned to different colors. At the strain of 0.00%, atoms at the grain boundary could not be recognized as any of the FCC, BCC,

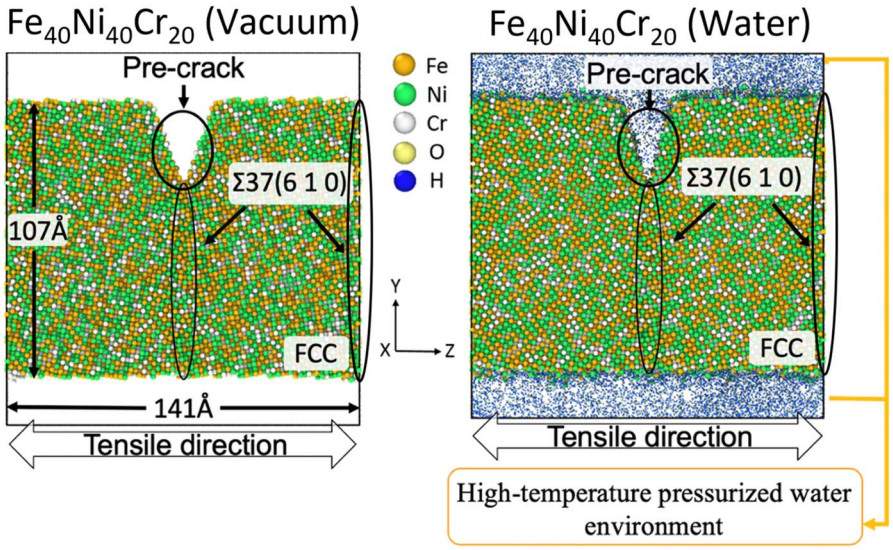

Fig. 1 Tensile simulation model of FCC-type $Fe_{40}Ni_{40}Cr_{20}$ alloy with a pre-crack at the Σ37 (610) grain boundary. A same grain boundary also appears at the cell edge.

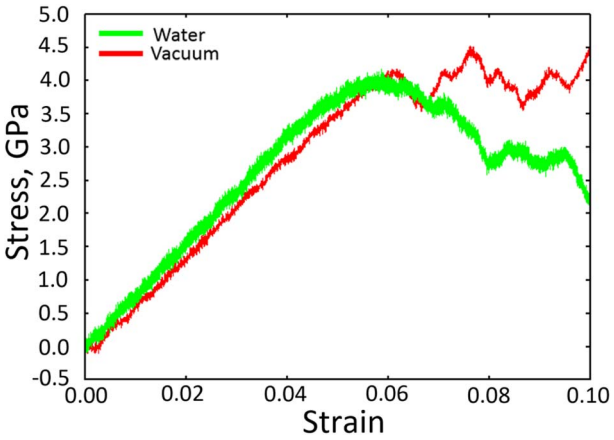

Fig. 2 Stress–strain curve of $Fe_{40}Ni_{40}Cr_{20}$ alloy in vacuum and high temperature/pressure water environments.

and HCP phases so that they are named as "others", while the rest atoms are recognized as FCC phase because the original $Fe_{40}Ni_{40}Cr_{20}$ alloy model is of FCC structure. In vacuum, there are some layered HCP phases beginning to generate from the grain boundary and surface at the strain of 5.50%, and then these layered HCP phases propagate and become more and more thick with the increase of tensile strain, as shown in Fig. 4a. We suggest that the generation of these HCP phases are the origin of the layered shear bands in Fig. 3a because their positions are totally the same. According to the crystallography analysis, these HCP phases are generated by the Shockley partial dislocation in FCC phase.[36] Fig. 5 schematically indicates the dislocation-induced phase transition from FCC (111) to HCP (001). In this illustration, blue, orange (both opaque and transparent ones), and red balls indicate the bottom, middle, and top layer atoms, respectively. For the normal FCC phase (right side of dislocation line), the top layer (red), middle layer (orange), and bottom layer (blue) are staggered with each other, and the black cube marks a typical FCC primitive cell where the opaque orange balls indicate the atoms of its (111) surface. When a Shockley partial dislocation is generated as shown in Fig. 5, the top layer (red) and middle layer (orange) atoms move downward with a Burgers vector of $\vec{b} = a/2$ where a is lattice constant, and hence the top layer (red) and bottom layer (blue) are overlapped becoming the HCP phase where the opaque orange balls indicate the atoms of its (001) surface. This illustration clearly shows the atomic mechanism of dislocation-induced phase transition from FCC (111) to HCP (001). Additionally, we found that these generated HCP layers are exactly parallel to the (111) surface of FCC matrix (see white lines in Fig. 3a), showing agreements with the above mechanism. In the case of high-temperature/pressure water environment, we observe the generation of BCC phase rather than HCP phase near the boundary at the strain of 5.50%. When the tensile strain increases to 8.50%, the BCC region becomes larger and larger, while a few layered HCP phases are generated from the boundary. These generated BCC and HCP phases are in the same positions with the areas of high atomic strain in Fig. 3b. We should notice that the water-induced change of deformation behavior (HCP layers to BCC blocks) is a universal behavior for Fe/Ni/Cr alloy, which is not affected by the change of element proportions. As the evidence, we have conducted tensile simulations of HEA with different element proportions ($Fe_{30}Ni_{30}Cr_{40}$, $Fe_{35}Ni_{35}Cr_{30}$, and $Fe_{30}Ni_{40}Cr_{30}$), as shown in Fig. S3–S5 of ESI.† All HEA models show similar tensile deformation results as that of $Fe_{40}Ni_{40}Cr_{20}$: layered HCP structures are generated in vacuum, whereas BCC phases are generated in water environment, confirming the universality of the above observed deformation mechanisms.

To clarify the unique deformation mechanism in water, we should first understand what happens at the alloy/water

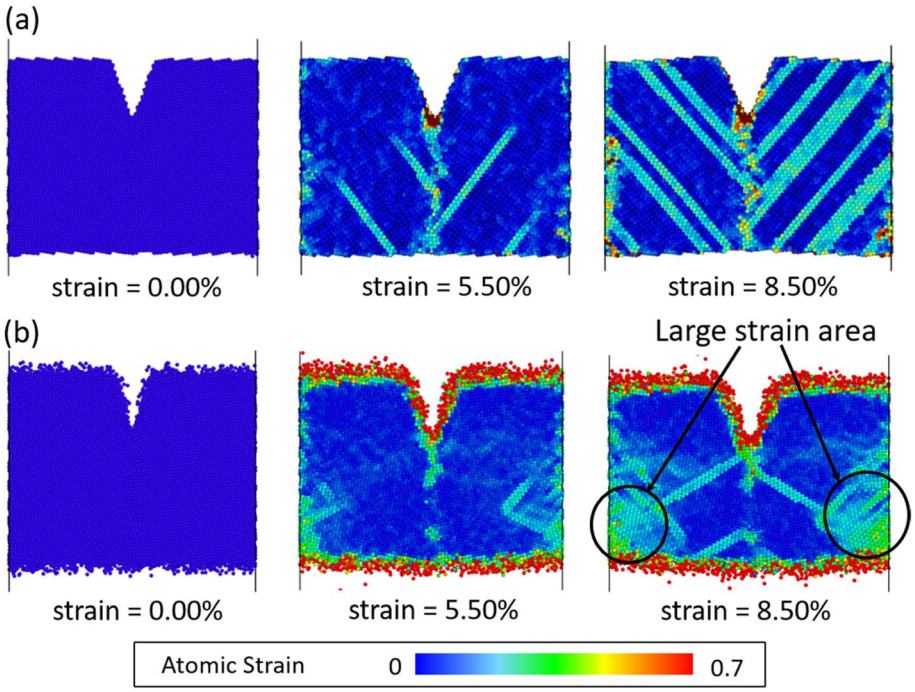

Fig. 3 Atomic shear strain of $Fe_{40}Ni_{40}Cr_{20}$ alloy in (a) vacuum and (b) high-temperature/pressure water environments. Non-reacted water molecules in (b) are invisible for clarity.

interface. Looking back the Fig. 3b and 4b again, it is noticed that the alloy surface in water becomes very rough while the atomic strains of surface atoms are very high. It is supposed that the alloy surface is oxidized by the chemical reactions with water molecules during tensile simulation. To verify this supposition, the numbers of chemical bonds including Fe–O, Ni–O, and Cr–O bonds are investigated as shown in Fig. 6. At the beginning of tensile simulation, the number of Cr–O, Fe–O, and Ni–O bonds are roughly 1850, 1200, and 700, respectively. This is because the alloy has been relaxed in water and the alloy surface is oxidized more or less before tensile simulation. As the numbers of Fe and Ni atoms are basically the same while the

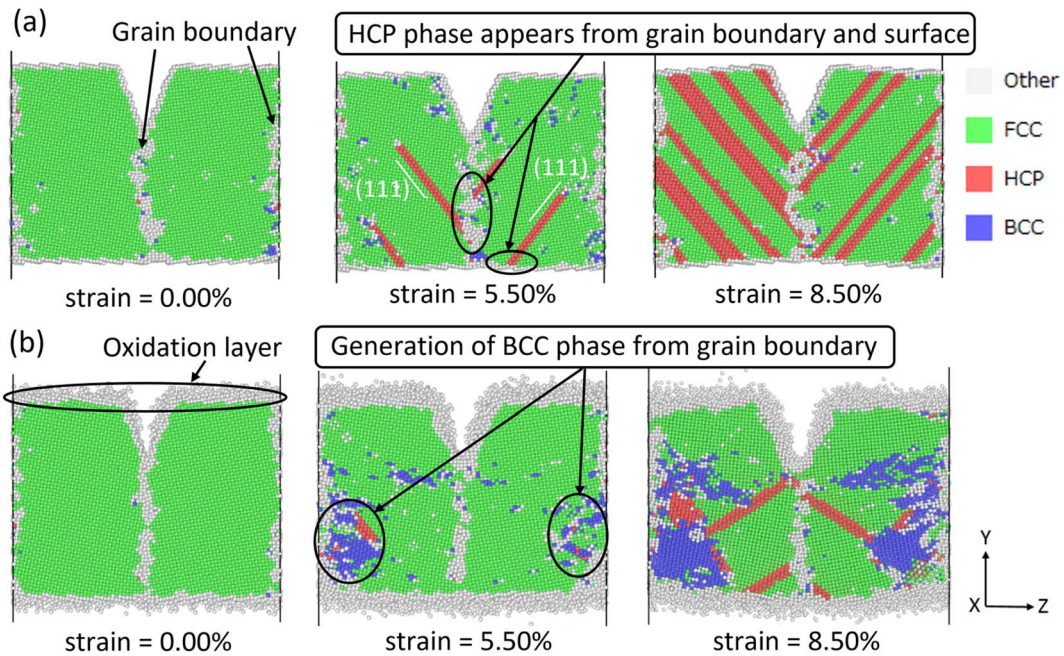

Fig. 4 Atomic structures of $Fe_{40}Ni_{40}Cr_{20}$ alloy in (a) vacuum and (b) high-temperature/pressure water environments.

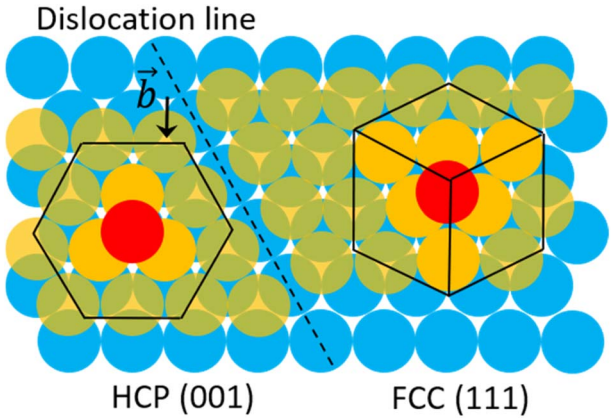

Fig. 5 Schematic illustration of the FCC-to-HCP phase transition mechanism induced by Shockley partial dislocation.

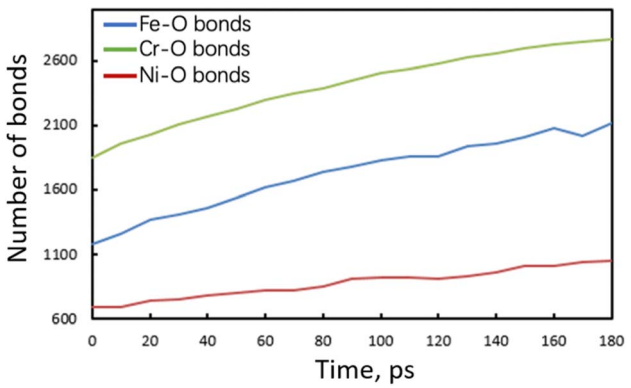

Fig. 6 Time evolution of the number of Fe–O, Ni–O, and Cr–O bonds of $Fe_{40}Ni_{40}Cr_{20}$ in high-temperature/pressure water environment.

number of Cr atoms is only a half of Fe (and Ni) atoms in $Fe_{40}Ni_{40}Cr_{20}$ alloy, we can conclude that Cr is most favorable to be oxidized following by Fe and Ni in sequence. This order of bond number corresponds to the electropositivity (antipode to electronegativity) of Cr, Fe, and Ni. With the proceeds of tensile simulation, the numbers of all Fe–O, Ni–O, and Cr–O bonds show a monotonic increasing trend, indicating a continuous oxidation of $Fe_{40}Ni_{40}Cr_{20}$ alloy surface by the reactions with water. The next question is how the surface oxidation correlates to the change of deformation mechanism? In vacuum, we have reported that the Shockley partial dislocation generated from surface and grain boundary causes the FCC-to-HCP phase transition. Thus, in the case of corrosive water environment, since the alloy surface is covered and passivated by an oxidized layer, the generation of Shockley partial dislocations from oxidized surface is surely suppressed, so that the alloy has to find another deformation pathway (which does not start from the surface) to release the tensile stress and stored elastic energy. The FCC-to-BCC phase transition may take place as one of the possible deformation mechanisms, as schematically shown in Fig. 7. The blue-line cuboid in Fig. 6 is of FCC phase initially, and it becomes the primitive cell of BCC when tensile strain of $\sqrt{2}-1$ is applied to both x and y directions. To sum up the deformation mechanism in water, chemical reactions between water molecules and alloy surface cause the surface oxidization and suppress the generation of Shockley partial dislocation from surface as well as the dislocation-induced FCC-to-HCP phase transition, so that the occurrence of FCC-to-BCC phase transition is preferred to release the tensile stress. Additionally, we should notice that the generation of dislocation from grain boundary is still possible even though surface is oxidized, and this is the reason why we can observe the generation of HCP phase from grain boundary at high tensile strain of 8.50%.

The changed deformation mechanism of $Fe_{40}Ni_{40}Cr_{20}$ alloy may well explain the distinct stress–strain curves and the elastic/plastic properties in both vacuum and high-temperature/pressure water environment (Fig. 2). The higher elastic modulus in water environment is because the $Fe_{40}Ni_{40}Cr_{20}$ alloy is difficult to deform *via* the FCC-to-HCP phase transition from surface by the surface oxidation. On the other hand, the lower ductility of $Fe_{40}Ni_{40}Cr_{20}$ alloy in water environment is because BCC phase is generally more brittle than FCC and HCP phases. Overall, the presence of high-temperature/pressure water causes the surface oxidation of $Fe_{40}Ni_{40}Cr_{20}$ alloy and hence changes the deformation mechanisms from FCC-to-HCP phase transition to FCC-to-BCC phase transition, which finally enhances the elastic modulus while reduce the ductility.

4. Conclusion

In this work, uniaxial tensile simulations of FCC-type $Fe_{40}Ni_{40}Cr_{20}$ alloy (as a simplified model of HEAs) are conducted in

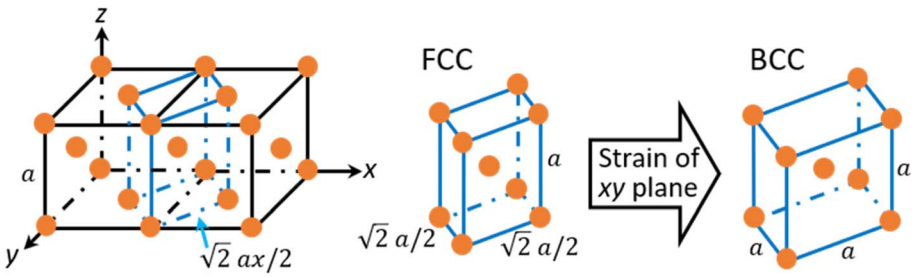

Fig. 7 Schematic illustration of the FCC-to-BCC phase transition.

vacuum and high-temperature/pressure water environment to clarify the effect of corrosive environment on the deformation mechanisms. In vacuum, layered HCP phases are formed from FCC matrix during tensile simulation due to the generation of Shockley partial dislocations from surface and grain boundary. While, in the corrosive water environment, alloy surface is oxidized by the reactions with water and this oxidized surface layer can suppress the generation of Shockley partial dislocation as well as the resulted FCC-to-HCP phase transition; instead, generation of BCC phase is preferred to release the tensile stress and stored elastic energy, leading to an enhanced elastic modulus and reduced ductility. Thus, we revealed that the deformation mechanism of $Fe_{40}Ni_{40}Cr_{20}$ alloy is changed by the presence of high-temperature/pressure water environment—from FCC-to-HCP phase transition in vacuum to FCC-to-BCC phase transition in water. This study as a theoretical fundamental may contribute to the further improvement of HEAs with high resistance to SCC in experiments.

Conflicts of interest

There are no conflicts to declare.

Acknowledgements

This research was supported by Japan Society for the Promotion Science (JSPS) Grant-in-Aid for Scientific Research on Innovative Areas "High Entropy Alloys" (Grant No. 18H05453), Scientific Research (B) (Grant No. 21H01235), Scientific Research (C) (Grant No. 19K05380 and 20K05147), and Research Fellow (Grant No. 19J21195), and by Japan Science and Technology Agency CREST (Grant No. JPMJCR2191). We gratefully acknowledge the Center for Computational Materials Science (CCMS, Tohoku University) for the use of Materials science Supercomputing system for Advances Multi-scale Simulations towards Next-generation – Institute for Materials Research (MASAMUNE-IMR) (Proposal No. 19S0506, 20S0509, and 202012-SCKXX-0502).

References

1 J. W. Yeh, S. K. Chen, S. J. Lin, J. Y. Gan, T. S. Chin, T. T. Shun, C. H. Tsau and S. Y. Chang, Nanostructured high-entropy alloys with multiple principal elements: Novel alloy design concepts and outcomes, *Adv. Eng. Mater.*, 2004, **6**, 299–303.

2 D. B. Miracle and O. N. Senkov, A critical review of high entropy alloys and related concepts, *Acta Mater.*, 2017, **122**, 448–511.

3 M. H. Tsai and J. W. Yeh, High-entropy alloys: A critical review, *Mater. Res. Lett.*, 2014, **2**, 107–123.

4 Y. Zhang, T. T. Zuo, Z. Tang, M. C. Gao, K. A. Dahmen, P. K. Liaw and Z. P. Lu, Microstructures and properties of high-entropy alloys, *Prog. Mater. Sci.*, 2014, **61**, 1–93.

5 J. Dong, X. Feng, X. Hao and W. Kuang, The environmental degradation behavior of FeNiMnCr high entropy alloy in high temperature hydrogenated water, *Scr. Mater.*, 2021, **204**, 114127.

6 S. Mizumachi, M. Koyama, Y. Fukushima and K. Tsuzaki, Growth behavior of a mechanically long fatigue crack in an FeCrNiMnCo high entropy alloy: A comparison with an austenitic stainless steel, *ISIJ Int.*, 2020, **60**, 175–181.

7 K. V. S. Thurston, B. Gludovatz, A. Hohenwarter, G. Laplanche, E. P. George and R. O. Ritchie, Effect of temperature on the fatigue-crack growth behavior of the high-entropy alloy CrMnFeCoNi, *Intermetallics*, 2017, **88**, 65–72.

8 M. S. Daw, S. M. Foiles and M. I. Baskes, The embedded-atom method: A review of theory and applications, *Mater. Sci. Rep.*, 1993, **9**, 251–310.

9 M. I. Baskes, Modified embedded-atom potentials for cubic materials and impurities, *Phys. Rev. B: Condens. Matter Mater. Phys.*, 1992, **46**, 2727–2742.

10 S. Li, X. Ding, J. Deng, T. Lookman, J. Li, X. Ren, J. Sun and A. Saxena, Superelasticity in bcc nanowires by a reversible twinning mechanism, *Phys. Rev. B: Condens. Matter Mater. Phys.*, 2010, **82**, 205435.

11 A. Ojha, H. Sehitoglu, L. Patriarca and H. J. Maier, Twin migration in Fe-based bcc crystals: Theory and experiments, *Philos. Mag.*, 2014, **94**, 1816–1840.

12 A. C. T. van Duin, S. Dasgupta and F. Lorant, ReaxFF: A reactive force field for hydrocarbons, *J. Phys. Chem. A*, 2001, **105**, 9396–9409.

13 T. P. Senftle, S. Hong, M. M. Islam, S. B. Kylasa, Y. Zheng, Y. K. Shin, C. Junkermeier, R. Engel-Herbert, M. J. Janik, H. M. Aktulga, T. Verstraelen, A. Grama and A. C. T. van Duin, The ReaxFF reactive force-field: Development, applications and future directions, *Npj Comput. Mater.*, 2016, **2**, 15011.

14 Y. Wang, N. Yamada, J. Xu, J. Zhang, Q. Chen, Y. Ootani, Y. Higuchi, N. Ozawa, M.-I. de Barros Bouchet, J. M. Martin, S. Mori, K. Adachi and M. Kubo, Triboemission of hydrocarbon molecules from diamond-like carbon friction interface induces atomic-scale wear, *Sci. Adv.*, 2019, **5**, eaax9301.

15 Y. Wang, Y. Su, J. Zhang, Q. Chen, J. Xu, S. Bai, Y. Ootani, N. Ozawa, M.-I. de Barros Bouchet, J. M. Martin, K. Adachi and M. Kubo, Reactive molecular dynamics simulations of wear and tribochemical reactions of diamond like carbon interfaces with nanoscale asperities under H_2 gas: Implications for solid lubricant coatings, *ACS Appl. Nano Mater.*, 2020, **3**, 7297–7304.

16 Y. Wang, J. Xu, Y. Ootani, N. Ozawa, K. Adachi and M. Kubo, Proposal of a new formation mechanism for hydrogenated diamond-like carbon transfer films: Hydrocarbon-emission-induced transfer, *Carbon*, 2019, **154**, 7–12.

17 Y. Wang, K. Yukinori, R. Koike, Y. Ootani, K. Adachi and M. Kubo, Selective wear behaviors of a water-lubricating SiC surface under rotating-contact conditions revealed by large-scale reactive molecular dynamics simulations, *J. Phys. Chem. C*, 2021, **125**, 14957–14964.

18 Y. Wang, J. Xu, Y. Ootani, N. Ozawa, K. Adachi and M. Kubo, Non-empirical law for nanoscale atom-by-atom wear, *Adv. Sci.*, 2021, **8**, 2002827.

19 J. Zhang, Y. Wang, Q. Chen, Y. Su, J. Xu, Y. Ootani, N. Ozawa, K. Adachi and M. Kubo, Graphitization dynamics of DLC under water lubrication revealed by molecular dynamics simulation, *J. Comput. Chem., Jpn.*, 2019, **18**, 103–104.

20 Q. Chen, J. Zhang, Z. Liu, Y. Wang, Y. Ootani, J. Xu, N. Ozawa and M. Kubo, Heterogeneous yielding mechanisms of body centered cubic iron for high resistance to chemical reaction-induced deterioration in supercritical water environments: A reactive molecular dynamics study, *Scr. Mater.*, 2021, **202**, 113997.

21 Y. Su, J. Zhang, Q. Chen, Y. Wang, N. Miyazaki, Y. Ootani, N. Ozawa and M. Kubo, A molecular dynamics study on alumina/carbon nanotube composite: How does annealing affect mechanical properties?, *J. Comput. Chem., Jpn.*, 2019, **18**, 259–262.

22 S. Monti, A. Corozzi, P. Fristrup, K. L. Joshi, Y. K. Shin, P. Oelschlaeger, A. C. T. van Duin and V. Barone, Exploring the conformational and reactive dynamics of biomolecules in solution using an extended version of the glycine reactive force field, *Phys. Chem. Chem. Phys.*, 2013, **15**, 15062–15077.

23 S. Keten, C. C. Chou, A. C. T. van Duin and M. J. Buehler, Tunable nanomechanics of protein disulfide bonds in redox microenvironments, *J. Mech. Behav. Biomed. Mater.*, 2012, **5**, 32–40.

24 K. Chenoweth, S. Cheung, A. C. T. van Duin, W. A. Goddard and E. M. Kober, Simulations on the thermal decomposition of a poly(dimethylsiloxane) polymer using the ReaxFF reactive force field, *J. Am. Chem. Soc.*, 2005, **127**, 7192–7202.

25 G. M. Odegard, B. D. Jensen, S. Gowtham, J. Wu, J. He and Z. Zhang, Predicting mechanical response of crosslinked epoxy using ReaxFF, *Chem. Phys. Lett.*, 2014, **591**, 175–178.

26 F. Otto, A. Dlouhý, C. Somsen, H. Bei, G. Eggeler and E. P. George, The influences of temperature and microstructure on the tensile properties of a CoCrFeMnNi high-entropy alloy, *Acta Mater.*, 2013, **61**, 5743–5755.

27 Z. Wu, H. Bei, G. M. Pharr and E. P. George, Temperature dependence of the mechanical properties of equiatomic solid solution alloys with face-centered cubic crystal structures, *Acta Mater.*, 2014, **81**, 428–441.

28 J. Xu, Y. Higuchi, N. Ozawa, K. Sato, T. Hashida and M. Kubo, Parallel large-scale molecular dynamics simulation opens new perspective to clarify the effect of a porous structure on the sintering process of Ni/YSZ multiparticles, *ACS Appl. Mater. Interfaces*, 2017, **9**, 31816–31824.

29 T. Pan and A. C. T. van Duin, Steel surface passivation at a typical ambient condition: Atomistic modeling and X-ray diffraction/reflectivity analyses, *Electrocatalysis*, 2011, **2**, 307–316.

30 Y. K. Shin, H. Kwak, A. v. Vasenkov, D. Sengupta and A. C. T. van Duin, Development of a ReaxFF reactive force field for Fe/Cr/O/S and application to oxidation of butane over a pyrite-covered Cr_2O_3 catalyst, *ACS Catal.*, 2015, **5**, 7226–7236.

31 Y. K. Shin, H. Kwak, C. Zou, A. van Vasenkov and A. C. T. van Duin, Development and validation of a ReaxFF reactive force field for Fe/Al/Ni alloys: Molecular dynamics study of elastic constants, diffusion, and segregation, *J. Phys. Chem. A*, 2012, **116**, 12163–12174.

32 L. Verlet, Computer "experiments" on classical fluids. I. thermodynamical properties of Lennard-Jones molecules, *Phys. Rev.*, 1967, **159**, 98–103.

33 L. Verlet, Computer "experiments" on classical fluids. II. equilibrium correlation functions, *Phys. Rev.*, 1968, **165**, 201–214.

34 D. J. Evans and B. L. Holian, The Nose-Hoover thermostat, *J. Chem. Phys.*, 1985, **83**, 4069–4074.

35 A. Stukowski, Visualization and analysis of atomistic simulation data with OVITO–the Open Visualization Tool, *Modell. Simul. Mater. Sci. Eng.*, 2009, **18**, 015012.

36 X. S. Yang, S. Sun, H. H. Ruan, S. Q. Shi and T. Y. Zhang, Shear and shuffling accomplishing polymorphic fcc $\gamma \rightarrow$ hcp $\varepsilon \rightarrow$ bct α martensitic phase transformation, *Acta Mater.*, 2017, **136**, 347–354.